Photocatalytic Decomposition of N₂O by Using Nanostructured Graphitic Carbon Nitride/Zinc Oxide Photocatalysts Immobilized on Foam

Kamila Kočí [1], Martin Reli [1], Ivana Troppová [1], Marcel Šihor [1,*], Tereza Bajcarová [2], Michal Ritz [2], Jiří Pavlovský [2] and Petr Praus [1,2]

[1] Institute of Environmental Technology, VŠB-Technical University of Ostrava, 17. listopadu 15, 708 00 Ostrava-Poruba, Czech Republic

[2] Faculty of Materials Science and Technology, VŠB-Technical University of Ostrava, 17. listopadu 15, 708 00 Ostrava-Poruba, Czech Republic

* Correspondence: marcel.sihor@vsb.cz; Tel.: +42-0597-327-304

Abstract: The aim of this work was to deposit cost-effective g-C₃N₄/ZnO nanocomposite photocatalysts (weight ratios of g-C₃N₄:ZnO from 0.05:1 to 3:1) as well as pure ZnO and g-C₃N₄ on Al₂O₃ foam and to study their photocatalytic efficiency for the photocatalytic decomposition of N₂O, which was studied in a home-made batch photoreactor under ultraviolet A irradiation (λ = 365 nm). Based on the photocatalysis measurements, it was found that photocatalytic decomposition of N₂O in the presence of all the prepared samples was significantly higher in comparison with photolysis. The photoactivity of the investigated nanocomposite photocatalysts increased in the following order: g-C₃N₄/ZnO (3:1) ≈ g-C₃N₄/ZnO (0.45:1) ≤ g-C₃N₄/ZnO (2:1) ZnO < g-C₃N₄ < g-C₃N₄/ZnO (0.05:1). The g-C₃N₄/ZnO (0.05:1) nanocomposite showed the best photocatalytic behavior and the most effective separation of photoinduced electron–hole pairs from all nanocomposites. The key roles played in photocatalytic activity were the electron–hole separation and the position and potential of the valence and conduction band. On the other hand, the specific surface area and band gap energy were not the significant factors in N₂O photocatalytic decomposition. Immobilization of the photocatalyst on the foam permits facile manipulation after photocatalytic reaction and their repeated application.

Keywords: carbon nitride; zinc oxide; alumina foam; photocatalysis; nitrous oxide

1. Introduction

Nitrous oxide is one of the most important greenhouse gases and represents 6.4% of the total global radiative forcing. Its contribution to global warming is important, because it is nearly 300 times higher than that of carbon dioxide [1]. N_2O is also a significant contributor to the destruction of the ozone layer in the stratosphere. The increase of N_2O emissions in the atmosphere (approximately 0.3% per year) is caused particularly by anthropogenic activities [1]. Synthetic nitrogen fertilizers in agriculture, combustion (fossil fuel, biomass), and the production of adipic acid and nitric acid are among the main contributors to N_2O emissions. The decomposition of nitrous oxide into N_2 and O_2 offers a simple method for its transformation to natural air elements. Decomposition of N_2O under UV irradiation on semiconductor materials (Equation (1)) is one possible solution for its removal:

$$N_2O \xrightarrow{h\nu, \; catalyst} N_2 + \frac{1}{2}O_2. \tag{1}$$

Photocatalytic decomposition of nitrous oxide was studied on Cu ions embedded on various oxides, e.g., ($SiO_2 \cdot Al_2O_3$, Al_2O_3, SiO_2) [2], ZnS [3], TiO_2 [4], TiO_2 doped by Ag [5–7], Ce [8,9].

Graphitic carbon nitride (g-C_3N_4) is an n-type semiconductor with a unique structure and useful optical, electric, and physicochemical properties. Although g-C_3N_4 has attracted increasing interest worldwide, its photocatalytic performance is still limited due to fast recombination of charge carriers [10–13]. Enhancing the photoactivity of g-C_3N_4-based photocatalysts can be achieved by the construction of semiconductors' heterojunctions [13,14]. The combination of different semiconductor photocatalysts may create new materials with optimal performances. The formation of unique semiconductor–semiconductor junctions can enhance the electron–hole separation for improved photocatalytic efficiency and extend the spectral range for light absorption. Looking into the mechanisms, one can identify that four dissimilar models of semiconductor–semiconductor junctions have been utilized to enhance the charge kinetics, including semiconductor sensitization, Type II, phase junction, and Z-scheme [15,16]. In our previous work, heterojunction photocatalysts (g-C_3N_4/TiO_2 and g-C_3N_4/WO_3 photocatalysts with various weight ratios) were prepared and studied for N_2O photocatalytic decomposition [17–19]. The formation of heterojunctions contributed to the increase of the N_2O conversion.

Recent investigations on semiconductors' photocatalysis are oriented to photocatalyst immobilization [16]. The immobilization of photocatalysts removes any imperfections with the powder form of the photocatalysts: (i) The difficulties of separating photocatalysts, (ii) the inclination of the nanoparticles of photocatalysts to aggregate, and (iii) the difficulty of applying them to continuous flow reactors [20].

For those reasons, we decided to prepare g-C_3N_4/ZnO nanocomposites with different weight ratios to immobilize them on Al_2O_3 foam, and to investigate them for N_2O photocatalytic decomposition under UVA (365 nm) irradiation. The g-C_3N_4/ZnO photocatalysts have not yet been studied for N_2O photocatalytic decomposition.

2. Results and Discussion

2.1. Photocatalysts Characterization

The real content of ZnO in prepared samples was determined by atomic absorption measurements (Table 1). The nitrogen physisorption characterization technique was used for the specific surface area determination (Figure 1). Each photocatalyst displayed a mesoporous-macroporous character. From the comparison of textural properties of the prepared samples, it is evident that the g-C_3N_4 addition positively affected the properties of the photocatalyst's porous structure, significantly enhancing its specific surface area as well as the net pore volume, e.g., pure ZnO showed a specific surface area of 7 m^2/g and a net pore volume of 61 mm^3_{liq}/g, while g-C_3N_4/ZnO (3:1) showed a specific surface area of 68 m^2/g and a net pore volume of 339 mm^3_{liq}/g (Table 1).
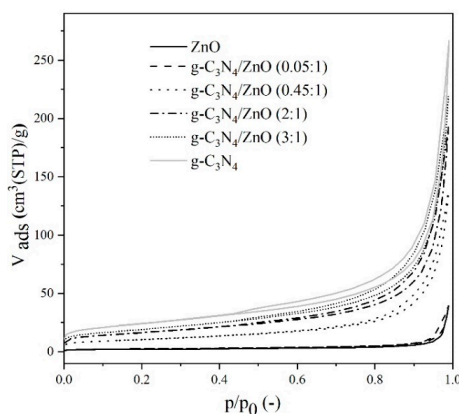
Figure 1. Nitrogen adsorption/desorption isotherms of ZnO, g-C_3N_4, and g-C_3N_4/ZnO.

Table 1. Structural and microstructural properties and content of ZnO ZnO, g-C$_3$N$_4$, and g-C$_3$N$_4$/ZnO.

Photocatalysts	S$_{BET}$ (m^2/g)	V net (mm$^3_{lig}$/g)	Content of Zn^{2+} (wt.%)
ZnO	7	61	80
g-C$_3$N$_4$/ZnO (0.05:1)	8	62	77
g-C$_3$N$_4$/ZnO (0.45:1)	37	212	55
g-C$_3$N$_4$/ZnO (2:1)	58	298	26
g-C$_3$N$_4$/ZnO (3:1)	68	339	21
g-C$_3$N$_4$	85	413	0

The X-ray powder diffraction (XRD) patterns of all investigated photocatalysts are shown in Figure 2. Two different phases based on zinc, zinc oxide, and zinc cyanamide were observed in all mixtures with higher contents of g-C$_3$N$_4$. The zinc oxide phase was markedly more significant than the zinc cyanide phase. Graphitic carbon nitride was confirmed by the presence of the reflection at position 14.9° 2Theta (d = 0.695 nm) indexed as the (100) plane and attributed to the in-plane tri-s-triazine units forming one-dimension melon strands. The most typical reflection was found around 32.2° 2Theta (d = 0.322 nm) and could be interpreted as long range interplanar stacking of the aromatic systems with the hkl plane (002). Unfortunately, this reflection was overlapped with the zinc cyanamide reflection (211) in all measured samples.

For the obtained g-C$_3$N$_4$/ZnO photocatalysts, nearly all of the characteristic diffraction peaks of zinc oxide were observed in the XRD pattern and confirmed the presence of the ZnO phase. In the case of the g-C$_3$N$_4$ phase, the (002) peak of g-C$_3$N$_4$ was almost not observed. The relatively poor crystallinity of the g-C$_3$N$_4$ phase indicates that simultaneous crystallization of the ZnO phase interferes with the condensation process and interlayer stacking patterns of the g-C$_3$N$_4$ phase, as shown by its weak diffraction intensity [21]. The XRD patterns in g-C$_3$N$_4$/ZnO photocatalysts indicate that these two phases occur separately in the composite and they do not have strong crystal lattice incorporation. This result was also confirmed by transmission electron microscopy (TEM).

All phases in the XRD patterns are marked by different symbols (Figure 2). All phases were identified using the PDF-2 database issued by the international center diffraction data. Zinc oxide corresponds to PDF-2 card no. 01-080-0075 and zinc cyanamide to PDF-2 card no. 01-070-4898. All XRD patterns were recorded using co-radiation with wavelength lambda = 1.78 Å. For this reason, all peaks were shifted to the higher 2Theta angles (based on the Braggs equation) than Cu radiation, which is more common.

(a)

(b)
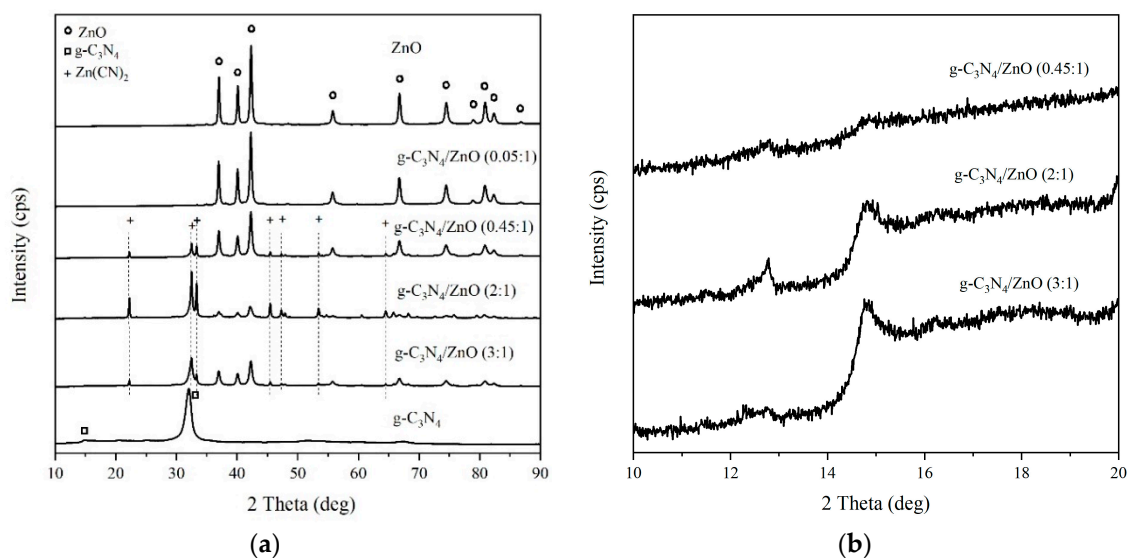
Figure 2. XRD patterns of ZnO, g-C$_3$N$_4$, and g-C$_3$N$_4$/ZnO (**a**) and XRD fragment of g-C$_3$N4/ZnO (0.45:1; 2:1, and 3:1) photocatalysts (**b**).

The UV–vis diffuse reflectance spectra of g-C$_3$N$_4$, ZnO, and g-C$_3$N$_4$/ZnO photocatalysts are compared in Figure 3a. The band gaps' energy values of the prepared nanocomposites were estimated by plotting the Kubelka–Munk function, as shown in Figure 3b. The largest band gap was 3.09 eV and it belongs to pure ZnO. On the other hand, pure g-C$_3$N$_4$ had a band gap energy of 2.64 eV. The nanocomposites band gap energies were 3.00, 2.75, 2.75, and 2.75 eV for g-C$_3$N$_4$/ZnO (0.05:1), g-C$_3$N$_4$/ZnO (0.45:1), g-C$_3$N$_4$/ZnO (2:1), and g-C$_3$N$_4$/ZnO (3:1), respectively. The presence of g-C$_3$N$_4$ in the nanocomposites extended the light absorption of the composites into the visible region compared to pure ZnO photocatalyst.
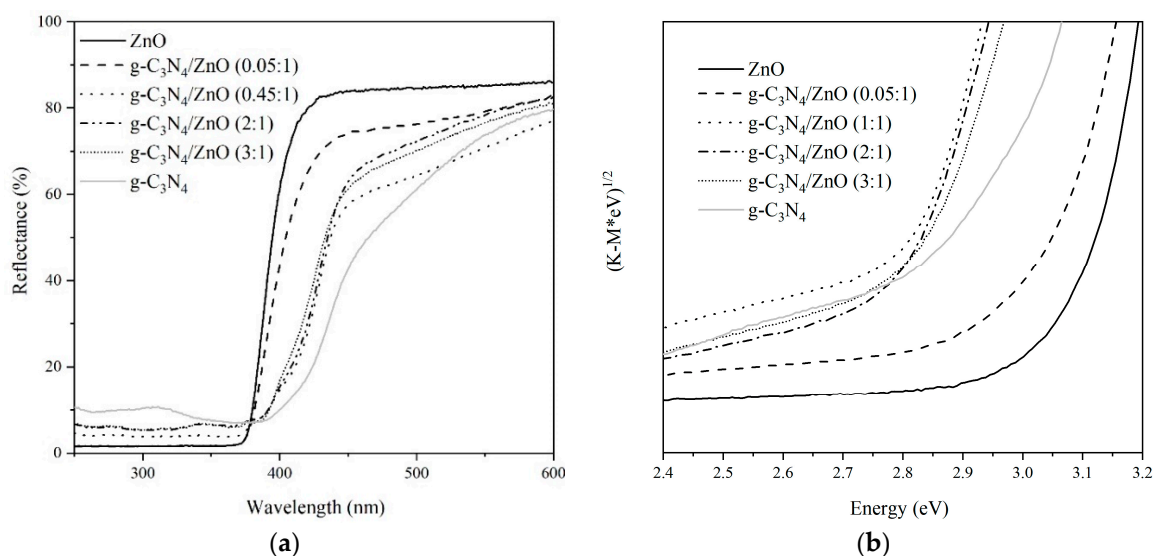

Figure 3. UV-vis diffuse reflectance spectra (**a**) and Tauc plots (**b**) of ZnO, g-C$_3$N$_4$, and g-C$_3$N$_4$/ZnO.

The infrared spectra are seen in Figure 4. The spectra of samples g-C$_3$N$_4$, g-C$_3$N$_4$/ZnO (3:1), g-C$_3$N$_4$/ZnO (2:1), and g-C$_3$N$_4$/ZnO (0.45:1) primarily contain bands that are characteristic for graphitic carbon nitride [22–24]. The regions are labelled as N1, N2, and N3. The region N1 contains bands at 3280, 3255, 3160, and 3090 cm^{-1}. These bands can be assigned to the stretching vibration of N-H bonds. The region N2 contains intensive bands at 1680 (shoulder), 1635, 1575, 1545, 1460, 1430 (shoulder), 1410, 1335 (shoulder), 1320, 1280, (shoulder), 1240, and 1210 cm^{-1}. Characteristic bands of the skeletal "breathing" vibration of aromatic rings of nitrogen heterocyclic compounds and stretching vibration bonds between carbon and nitrogen were found in the N2 region. The N3 region contains only a medium intensive band at 815 cm^{-1}, which is due to the breathing mode of the triazine unit. Moreover, the spectra of samples g-C$_3$N$_4$/ZnO (3:1), g-C$_3$N$_4$/ZnO (2:1), and g-C$_3$N$_4$/ZnO (0.45:1) also contain bands of complex cyanide compounds at 2085 and 2045 cm^{-1} [25]. The bands have a medium or weak intensity (see region CN). The relative red shifts of the complex cyanide compounds compared with the normal wavenumber of 2250 cm^{-1} are due to the conjugation effect of the extended C-N aromatic system [21]. The spectra of samples g-C$_3$N$_4$/ZnO (0.05:1) and ZnO only contain medium or weak bands of carbonates (see region C1 and C2) and a broad band of zinc oxide (see region Z). The carbonate bands can be assigned to asymmetric stretching vibration of carbonate (1450 cm^{-1}) and symmetric deformation vibration of carbonate (885 cm^{-1}), respectively [25]. The band of vibration of zinc oxide [26] is seen at 480 cm^{-1}. This band is seen also in the spectrum of sample g-C$_3$N$_4$/ZnO (0.45:1).
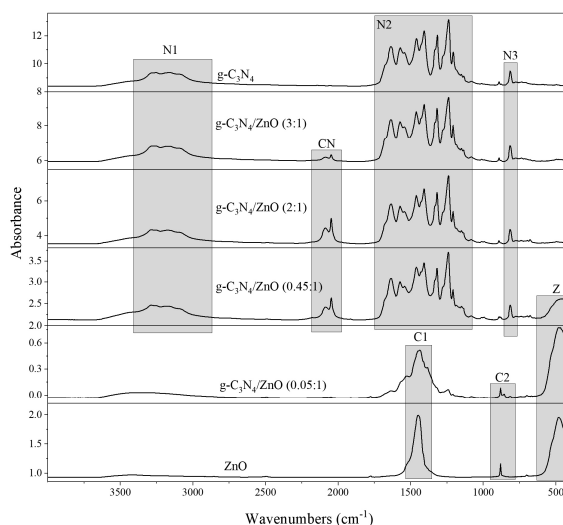
Figure 4. Infrared spectra of ZnO, g-C_3N_4, and g-C_3N_4/ZnO.

The Raman spectra are seen in Figure 5. The spectra are in the "full-scale" mode, thus the presented spectra have different scales of intensity axes. The spectra of samples g-C_3N_4, g-C_3N_4/ZnO (3:1), g-C_3N_4/ZnO (2:1), and g-C_3N_4/ZnO (0.45:1) only contain the bands characteristic for graphitic carbon nitride (i.e., [22,24,27]) in the regions labelled N1, N2, N3, N4, and N5. The N1 region contains strong bands at 1230 and 1215 cm^{-1} and weak bands at 1150 and 1115 cm^{-1}. The N2 region contains a medium band at 770 cm^{-1} and a strong band at 705 cm^{-1}. The N3 region contains two medium bands at 485 and 470 cm^{-1} and one weak band at 455 cm^{-1}. Medium bands at 355 and 210 cm^{-1} are in the N4 and N5 regions, respectively. The assignment of the above-mentioned Raman bands of graphitic carbon nitride has not been published yet. We can suppose the bands are related to vibration of the tri-s-triazine ring (i.e., [27]). The spectra of samples g-C_3N_4/ZnO (0.05:1) and ZnO contain two bands of carbonate (see region C1 and C2) and three bands of zinc oxide (see region Z1, Z2, and Z3). The carbonate bands are presented at 1080 cm^{-1} (symmetric stretching vibration) and at 700 cm^{-1} (symmetric deformation vibration), respectively [25]. The bands characteristic for zinc oxide are presented at 435, 330, and 185 cm^{-1}.
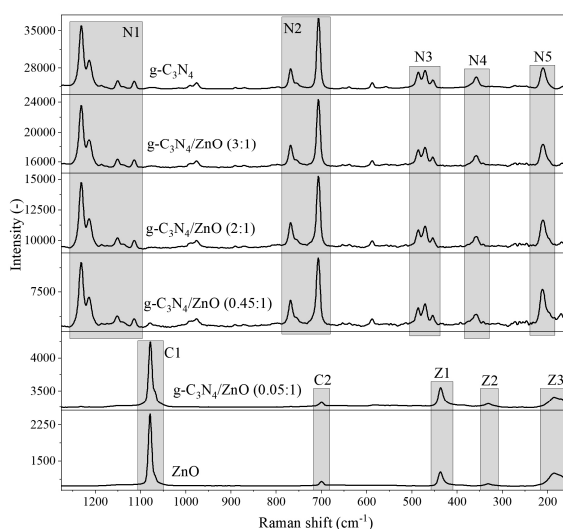

Figure 5. Raman spectra of ZnO, g-C_3N_4, and g-C_3N_4/ZnO.

Figure 6a–d demonstrate the TEM images of pure ZnO, g-C_3N_4, and g-C_3N_4/ZnO (3:1) photocatalysts, respectively. The ZnO nanoparticles (Figure 6a) have hexagonal shapes and the

particle size is about 50 nm while pure g-C_3N_4 (Figure 6b) shows a 2D lamellar structure. The TEM micrographs of g-C_3N_4/ZnO (3:1) (Figure 6c) testify that the ZnO nanoparticles were not supported well on the surface of g-C_3N_4. It is possible to infer that the salt (from preparation) can be observed in the g-C_3N_4/ZnO samples (Figure 6d). It is also evident from the results of the EDS analysis (Figure 6e), which confirmed not only the presence of Zn, C, O, and N elements but also Na element. The presence of the salt was also confirmed by Raman and infrared spectroscopy.
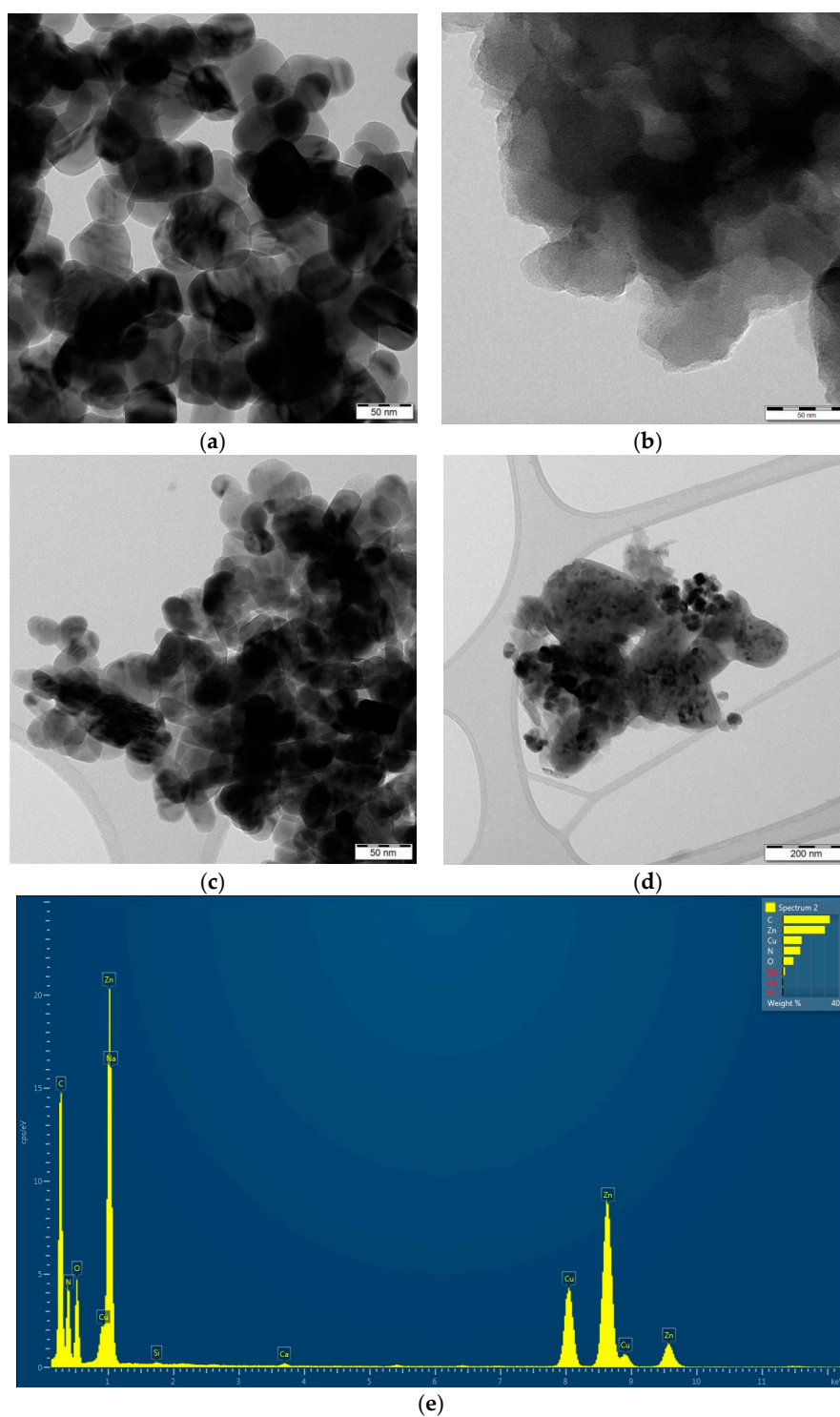

Figure 6. TEM images of ZnO (**a**), g-C_3N_4 (**b**), and g-C_3N_4/ZnO (3:1) (**c**,**d**) and EDS analysis of g-C_3N_4/ZnO (3:1) (**e**).

Photoelectrochemical measurements of all photocatalysts are shown in Figure 7. It is evident that the magnitude of the generated current decreased with an increasing amount of g-C_3N_4 presented at the photocatalysts until the g-C_3N_4 was in the majority. Higher photocurrents measured in the presence of the ZnO sample show that there are significantly more charge carriers produced in ZnO compared to g-C_3N_4. The photocurrent decreased with an increasing amount of g-C_3N_4, which formed a significantly smaller photocurrent.

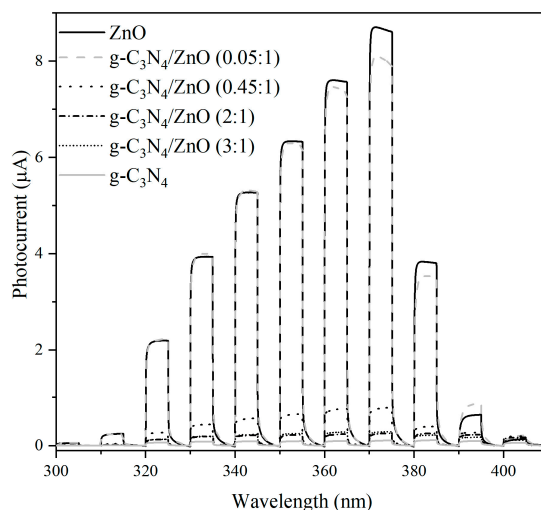**Figure 7.** Photocurrent generation at electrodes made of ZnO, g-C_3N_4, and g-C_3N_4/ZnO recorded at 1 V vs. Ag/AgCl in deoxygenated 0.1 M KNO_3.

2.2. Photocatalytic Decomposition of N_2O

The influence of prepared nanocomposites on the photocatalytic decomposition of nitrous oxide was studied from 0 to 22 h (Figure 8). The photolysis was also conducted in order to confirm the photocatalytic activity of the prepared samples. The time dependences of the nitrous oxide conversion of all g-C_3N_4/ZnO nanocomposites, including pure ZnO and g-C_3N_4 photocatalysts, are depicted in Figure 8. It is evident that each prepared photocatalyst proved to be much more effective in comparison with photolysis. The g-C_3N_4/ZnO (0.05:1) and pure g-C_3N_4 and ZnO showed a significantly higher efficiency than other photocatalysts.

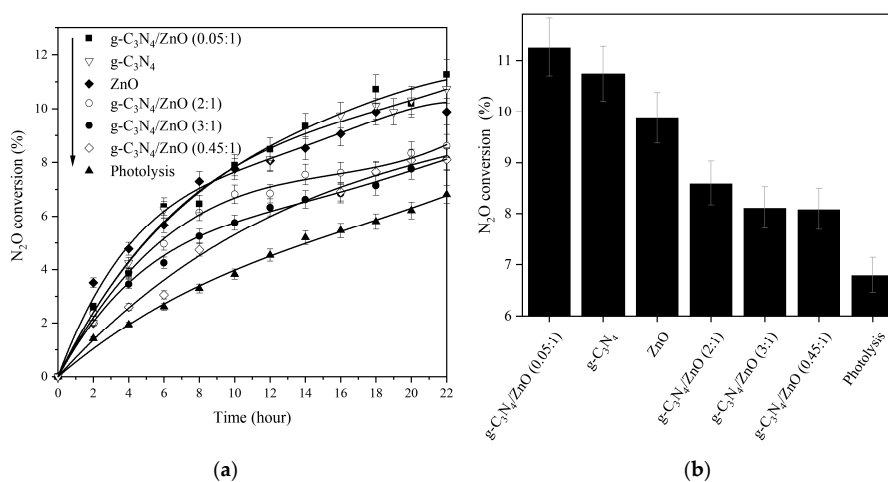**Figure 8.** The time dependences of N_2O conversion (**a**) and N_2O conversion after 22 h of irradiation (**b**) over ZnO, g-C_3N_4 and g-C_3N_4/ZnO and photolysis under UVA (λ = 365 nm) irradiation.

The highest N_2O conversion under UVA irradiation was reached over the g-C_3N_4/ZnO (0.05:1) photocatalyst. The N_2O conversion in the presence of this photocatalyst was 11% after 22 h of UVA irradiation. For comparison, the N_2O conversion without photocatalyst was only 6% after 22 h of UVA irradiation. The same foam with photocatalyst was used for repeated tests three times. This confirms the stability and ability to reuse these materials without losing photocatalytic activity.

It is hard to compare the observed photocatalytic results with the literature, as it is usually measured under different reaction conditions (geometry of photoreactor, irradiation source, concentration of N_2O, amount of photocatalyst, whether it is immobilized, and also the irradiation time). Each of these conditions influences the photocatalytic decomposition of N_2O in a different way and therefore accurate comparison is impossible. Also, not many research groups have investigated the photocatalytic decomposition of N_2O. Therefore, the obtained results were compared with our previous works. N_2O conversion for the g-C_3N_4/$BiVO_4$ and g-C_3N_4/WO_3 composites after 20 h of irradiation was 12.5% and 14.5%, respectively. However, both previous sets of photocatalysts were measured in a different photoreactor (different geometry) and therefore, from that point of view, the observed N_2O conversion of approximately 10% after 20 h of irradiation seems to be comparable to the previous results.

2.3. Proposed Mechanism for Photocatalytic Activity Enhancement

When g-C_3N_4 is combined with ZnO, the generated electrons (e^-) and holes (h^+) can migrate by two possible mechanisms: Type II heterojunction and the Z-scheme system. In the case of the type II heterojunction of g-C_3N_4/ZnO, the generated e^- in the conduction band (CB) of g-C_3N_4 can transfer to the CB of ZnO and simultaneously, the h^+ in the valence band (VB) of ZnO can migrate to the VB of g-C_3N_4. In the case of the Z-scheme system of g-C_3N_4/ZnO, e^- in the CB of ZnO are directly recombined with the h^+ in the VB of g-C_3N_4 at the heterojunction interface, and so the recombination of e^- and h^+ in ZnO and g-C_3N_4 is inhibited. In this case, the e^- are accumulated in the CB of g-C_3N_4 and h^+ in the VB of ZnO. Due to these two mechanisms, a prolonged lifetime of electrons and holes is gained [14].

The band edge positions of materials were calculated via Equations (2) and (3) [28]:

$$E_{VB} = \chi - E_0 + 0.5E_g, \tag{2}$$

$$E_{CB} = E_{VB} - E_g, \tag{3}$$

where χ is the electronegativity of the material, E_{VB} is the VB potential, E_{CB} is the CB potential, E_g is the band gap energy of a material, and E_0 is the energy of free electrons (4.5 V vs. NHE). The χ values for g-C_3N_4 and ZnO are 4.72 and 5.95 eV, respectively [28]. The E_{VB} of g-C_3N_4 and ZnO were 1.75 and 3.05 eV, respectively. The E_{CB} of g-C_3N_4 and ZnO were −1.31 and −0.15 V, respectively.

The formation of the Z-scheme system of g-C_3N_4/ZnO can be confirmed by the hydroxyl radical (•OH) trapping test using modified photoluminescence (PL) measurements [29]. After the photoexcitation, the h^+ with sufficient oxidation potential can be either directly involved in the photocatalytic degradation reactions or generate active species. The reaction between terephthalic acid (TA) and hydroxyl radicals (•OH) can generate hydroxyterephthalic acid (HTA), which is detectable by the PL spectrometer (signal with maximal intensity centered at 425 nm) [30]. The PL peak intensity of the HTA is in proportion to the amount of produced •OH.

Since the photoluminescence intensity increased in the presence of each photocatalyst over time, with the exception of pure g-C_3N_4, the presence of hydroxyl radicals was confirmed (Figure 9a). According to the band structures of ZnO and g-C_3N_4, the photoinduced h^+ on g-C_3N_4 cannot oxidize the adsorbed H_2O molecules to •OH because the VB potential of g-C_3N_4 (+1.75 V vs. NHE) is less positive than the standard redox potential of •OH/OH^- (2.4 V vs. NHE). In the case of Z-scheme formation, the photogenerated h^+ remain on the ZnO. The h^+ accumulation on ZnO is in accordance with the migration mechanism of the direct Z-scheme. The creation of the Z-scheme system was observed by Wang et al. [14], Liu et al. [31], and Yu et. al. [21]. In our case, it was not confirmed that

g-C$_3$N$_4$/ZnO nanocomposite had contact with the Z-scheme system because the nanocomposites were not proven to have a higher PL intensity than pure ZnO. The PL intensity decreased with an increasing content of ZnO, which can produce hydroxyl radical.
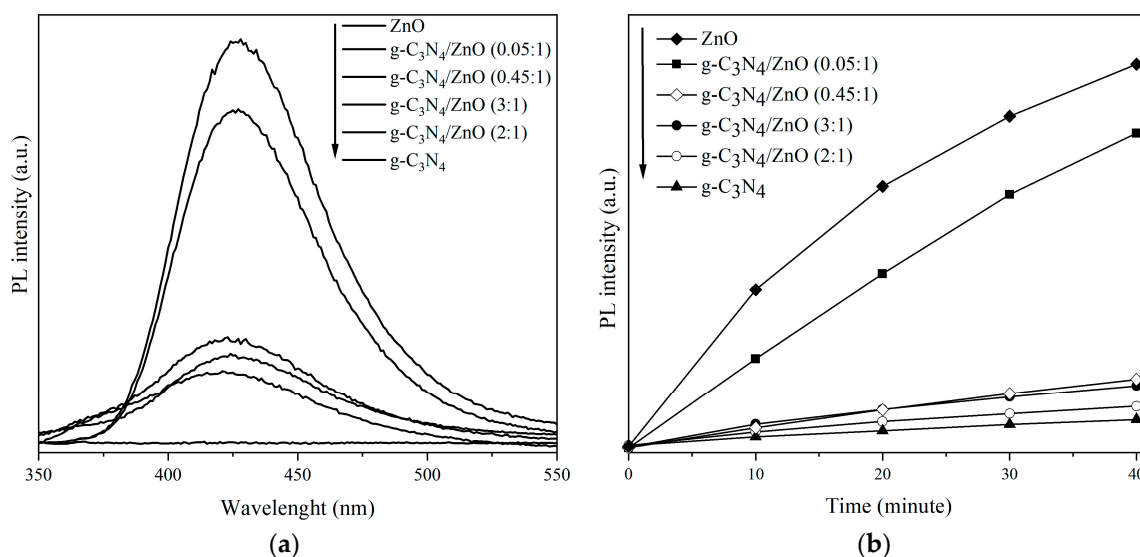

Figure 9. PL spectra in presence of TA in NaOH solution (excitation wave: 365 nm), irradiated for 40 min in the presence of ZnO, g-C$_3$N$_4$, and g-C$_3$N$_4$/ZnO (**a**) and a comparison of the PL intensity against irradiation time for of g-C$_3$N$_4$/ZnO nanocomposites (**b**).

According to the literature, the standard reduction potential of N$_2$O/N$_2$ is +1.355 V [32]. The conduction bands' potentials of both pure and prepared photocatalysts (g-C$_3$N$_4$ and ZnO) are more negative (−1.19 and −0.17 V, respectively) than the standard reduction potential of N$_2$O/N$_2$. Therefore, both pure photocatalysts showed similar photocatalytic activity.

The photocatalytic activity of g-C$_3$N$_4$/ZnO, with the exception of g-C$_3$N$_4$/ZnO (0.05:1), was lower with regard to pure photocatalysts. These three nanocomposites (g-C$_3$N$_4$/ZnO (0.45:1), g-C$_3$N$_4$/ZnO (2:1), and g-C$_3$N$_4$/ZnO (3:1)) had not only similar photocatalytic activity but also band gap energy. The photocatalytic activity of nanocomposites (g-C$_3$N$_4$/ZnO (0.45:1), g-C$_3$N$_4$/ZnO (2:1), and g-C$_3$N$_4$/ZnO (3:1)) decreased both by the presence of cyanide compounds formed during preparation (Figure 4) and by the imperfect contact of g-C$_3$N$_4$ and ZnO, which is visible in Figure 6c. The detection of cyanide compounds in g-C$_3$N$_4$/ZnO indicates that simultaneous ZnO crystallization could interfere with the thermal polymerization of melamine to generate a well-defined g-C$_3$N$_4$ phase. Based on the previous discussion about XRD patterns and infrared spectra, such interference in ZnO crystallization can result in relatively poor crystallinity and give rise to defect states within the g-C$_3$N$_4$ phase [21]. These defect states can catch generated charge carriers; however, they are not accessible for the adsorbed molecule of nitrous oxide, which consequently leads to a decrease in photoactivity.

A slightly different situation is the case of g-C$_3$N$_4$/ZnO (0.05:1), which proved to have the highest photocatalytic activity. This nanocomposite contained only 4% of g-C$_3$N$_4$, which means most of the holes in VB of g-C$_3$N$_4$ probably recombined with some of the electrons from the CB of ZnO. In the meantime, the photogenerated electrons in the CB of g-C$_3$N$_4$ and a big part of the electrons in the CB of ZnO, which was not used for recombination with holes of g-C$_3$N$_4$, reduced N$_2$O to N$_2$ and •O$^-$. The photoexcited holes in the VB of ZnO oxidized •O$^-$ to O$_2$ [19]. This result shows that only a small loading of g-C$_3$N$_4$ in g-C$_3$N$_4$/ZnO can increase the effectiveness of photogenerated electron–hole separation.

In heterogeneous photocatalysis, on the contrary to catalysis, the specific surface (S$_{BET}$) is not the most crucial parameter. It is obvious in this work, where g-C$_3$N$_4$/ZnO (0.05:1) and g-C$_3$N$_4$ had a similarly high photoactivity though the S$_{BET}$ of g-C$_3$N$_4$ was more than 10 times higher than in the case

of g-C$_3$N$_4$/ZnO (0.05:1). Many authors have quoted the band gap energy as one of the most important parameters. The photoelectrochemical measurements validated the capability of all nanocomposites to absorb UVA. Moreover, both pure photocatalysts, which had similar photoactivity, have different band gap energy. Consequently, the band gap energy is not the most decisive parameter. The most significant factor, which is valid in photocatalytic reactions generally, is the position and potential of the valence and conduction band.

3. Materials and Methods

3.1. Preparation of ZnO, g-C$_3$N$_4$, and g-C$_3$N$_4$/ZnO Nanocomposites

ZnO was prepared by precipitation [33]. G-C$_3$N$_4$ was formed by heating of melamine [18,34]. In a synthesis procedure of g-C$_3$N$_4$/ZnO, the determined amounts of ZnO and g-C$_3$N$_4$ were dispersed in deionized water and evenly mixed (4 h). Subsequently, the mixture was dried (at 60 °C in air) and calcined [18]. The weight ratios of prepared g-C$_3$N$_4$/ZnO photocatalysts were set at 0.05:1, 0.45:1, 2:1, and 3:1, respectively. The prepared nanocomposites (0.1 g) were anchored on a commercial support VUKOPOR (Lanik Ltd., Boskovice, Czech Republic) [35,36]. For detailed preparation information, see the Supplementary Materials.

3.2. Characterization of g-C$_3$N$_4$/ZnO Nanocomposite and Photocatalytic Decomposition of N$_2$O

The products were characterized in detail by N$_2$ physisorption (Micromeritics), X-ray powder diffraction (XRD, Rigaku, Tokyo, Japan), UV–Vis diffuse reflectance spectra (DRS, IRS-2600Plus), transmission electron microscopy (TEM, JEOL 2100 equipped with an EDS detector, Tokyo, Japan), Fourier transform infrared spectroscopy (FT-IR, Nexus 470 ThermoScientific, Waltham, MA, USA), Raman spectroscopy (DXR SmartRaman (ThermoScientific), photoluminescence (PL) measurements (FLSP920 Series, Edinburgh Instruments, Livingston, UK), and photoelectrochemical measurements (Instytut Fotonowy, Krakow, Poland), and their photocatalytic activity was studied for the photocatalytic decomposition of N$_2$O according to the reported method [18,29]. The photocatalytic inactivity of the bare foam was confirmed via blank tests and compared to the blank test without foam.

4. Conclusions

g-C$_3$N$_4$/ZnO nanocomposites with different ratios of components as well as pure ZnO and g-C$_3$N$_4$ were prepared with success. Each photocatalyst was coated on commercial Al$_2$O$_3$ foam. The prepared nanocomposites were investigated for N$_2$O photocatalytic decomposition for the first time. g-C$_3$N$_4$ addition positively affects the properties of the photocatalysts' porous structure, significantly enhancing its specific surface area as well as the net pore volume. In all mixtures with higher contents of g-C$_3$N$_4$, two phases based on zinc were observed, -zinc oxide (markedly more significant) and zinc cyanamide. ZnO nanoparticles have hexagonal shapes and pure g-C$_3$N$_4$ shows a 2D lamellar structure. Based on the experimental and characterization results, N$_2$O conversion in the presence of photocatalysts was higher in comparison with photolysis; in the case of the best photocatalysts, g-C$_3$N$_4$/ZnO (0.05:1) was almost twice higher. FT-IR characterization showed that samples of the g-C$_3$N$_4$/ZnO (3:1), g-C$_3$N$_4$/ZnO (2:1), and g-C$_3$N$_4$/ZnO (0.45:1) photocatalysts also contained cyanide compounds, which together with an imperfect contact of g-C$_3$N$_4$ and ZnO caused a decrease of photocatalytic activity. The key role played in photocatalytic activity was the electron–hole separation and the position and potential of the valence and conduction band. On the other hand, the specific surface area and band gap energy were not significant factors in N$_2$O photocatalytic decomposition. The immobilization on commercial Al$_2$O$_3$ foam proved to be promising. A short-term test confirmed the photocatalysts' stability and reproducible activity. Immobilization might be an efficient way to bring photocatalysis closer to an application, since the powder form is not usable for several reasons, such as filtration from the liquid phase or blowing off by the gas stream. No such drawbacks exist with the immobilized photocatalyst on the foam.

References

1. Ming, T.; de Richter, R.; Shen, S.; Caillol, S. Fighting global warming by greenhouse gas removal: Destroying atmospheric nitrous oxide thanks to synergies between two breakthrough technologies. *Environ. Sci. Pollut. Res. Int.* **2016**, *23*, 6119–6138. [CrossRef] [PubMed]

2. Matsuoka, M.; Ju, W.S.; Takahashi, K.; Yamashita, H.; Anpo, M. Photocatalytic decomposition of N_2O into N_2 and O_2 at 298 K on Cu(I) ion catalysts anchored onto various oxides. The effect of the coordination state of the Cu(I) ions on the photocatalytic reactivity. *J. Phys. Chem. B* **2000**, *104*, 4911–4915. [CrossRef]

3. Obalová, L.; Šihor, M.; Praus, P.; Reli, M.; Kočí, K. Photocatalytic and photochemical decomposition of N_2O on ZnS-MMT catalyst. *Catal. Today* **2014**, *230*, 61–66. [CrossRef]

4. Kočí, K.; Matějová, L.; Obalová, L.; Čapek, L.; Wu, J.C.S. Preparation, characterization and photocatalytic performance of TiO_2 prepared by using pressurized fluids in CO_2 reduction and N_2O decomposition. *J. Sol Gel Sci. Technol.* **2015**, *76*, 621–629. [CrossRef]

5. Sano, T.; Negishi, N.; Mas, D.; Takeuchi, K. Photocatalytic Decomposition of N_2O on Highly Dispersed Ag+ Ions on TiO_2 Prepared by Photodeposition. *J. Catal.* **2000**, *194*, 71–79. [CrossRef]

6. Kočí, K.; Krejčíková, S.; Šolcová, O.; Obalová, L. Photocatalytic decomposition of N_2O on Ag-TiO_2. *Catal. Today* **2012**, *191*, 134–137. [CrossRef]

7. Obalová, L.; Reli, M.; Lang, J.; Matějka, V.; Kukutschová, J.; Lacný, Z.; Kočí, K. Photocatalytic decomposition of nitrous oxide using TiO_2 and Ag-TiO_2 nanocomposite thin films. *Catal. Today* **2013**, *209*, 170–175. [CrossRef]

8. Matějová, L.; Šihor, M.; Brunátová, T.; Ambrožová, N.; Reli, M.; Čapek, L.; Obalová, L.; Kočí, K. Microstructure-performance study of cerium-doped TiO_2 prepared by using pressurized fluids in photocatalytic mitigation of N_2O. *Res. Chem. Intermed.* **2015**, *41*, 9217–9231. [CrossRef]

9. Kočí, K.; Matějová, L.; Ambrožová, N.; Šihor, M.; Troppová, I.; Čapek, L.; Kotarba, A.; Kustrowski, P.; Hospodková, A.; Obalová, L. Optimization of cerium doping of TiO_2 for photocatalytic reduction of CO_2 and photocatalytic decomposition of N_2O. *J. Sol Gel Sci. Technol.* **2016**, *78*, 550–558. [CrossRef]

10. Prasad, C.; Tang, H.; Bahadur, I. Graphitic carbon nitride based ternary nanocomposites: From synthesis to their applications in photocatalysis: A recent review. *J. Mol. Liq.* **2019**, *281*, 634–654. [CrossRef]

11. Yin, S.; Han, J.; Zhou, T.; Xu, R. Recent progress in g-C_3N_4 based low cost photocatalytic system: Activity enhancement and emerging applications. *Catal. Sci. Technol.* **2015**, *5*, 5048–5061. [CrossRef]

12. Masih, D.; Ma, Y.; Rohani, S. Graphitic C_3N_4 based noble-metal-free photocatalyst systems: A review. *Appl. Catal. B Environ.* **2017**, *206*, 556–588. [CrossRef]

13. Wen, J.; Xie, J.; Chen, X.; Li, X. A review on g-C_3N_4-based photocatalysts. *Appl. Surf. Sci.* **2017**, *391*, 72–123. [CrossRef]

14. Wang, J.; Xia, Y.; Zhao, H.; Wang, G.; Xiang, L.; Xu, J.; Komarneni, S. Oxygen defects-mediated Z-scheme charge separation in g-C_3N_4/ZnO photocatalysts for enhanced visible-light degradation of 4-chlorophenol and hydrogen evolution. *Appl. Catal. B* **2017**, *206*, 406–416. [CrossRef]

15. Low, J.; Cheng, B.; Yu, J. Surface modification and enhanced photocatalytic CO_2 reduction performance of TiO_2: A review. *Appl. Surf. Sci.* **2017**, *392*, 658–686. [CrossRef]

16. Bai, S.; Jiang, J.; Zhang, Q.; Xiong, Y. Steering charge kinetics in photocatalysis: Intersection of materials syntheses, characterization techniques and theoretical simulations. *Chem. Soc. Rev.* **2015**, *44*, 2893–2939. [CrossRef] [PubMed]

17. Reli, M.; Huo, P.; Sihor, M.; Ambrozova, N.; Troppova, I.; Matejova, L.; Lang, J.; Svoboda, L.; Kustrowski, P.; Ritz, M.; et al. Novel TiO_2/C_3N_4 Photocatalysts for Photocatalytic Reduction of CO_2 and for Photocatalytic Decomposition of N_2O. *J. Phys. Chem. A* **2016**, *120*, 8564–8573. [CrossRef] [PubMed]

18. Kočí, K.; Reli, M.; Troppová, I.; Šihor, M.; Kupková, J.; Kustrowski, P.; Praus, P. Photocatalytic decomposition of N_2O over TiO_2/g-C_3N_4 photocatalysts heterojunction. *Appl. Surf. Sci.* **2017**, *396*, 1685–1695. [CrossRef]

19. Reli, M.; Svoboda, L.; Šihor, M.; Troppová, I.; Pavlovský, J.; Praus, P.; Kočí, K. Photocatalytic decomposition of N_2O over g-C_3N_4/WO_3 photocatalysts. *Environ. Sci. Pollut. Res. Int.* **2018**, *25*, 34839–34850. [CrossRef]

20. Alenzi, N.; Liao, W.-S.; Cremer, P.S.; Sanchez-Torres, V.; Wood, T.K.; Ehlig-Economides, C.; Cheng, Z. Photoelectrochemical hydrogen production from water/methanol decomposition using Ag/TiO_2 nanocomposite thin films. *Int. J. Hydrogen Energy* **2010**, *35*, 11768–11775. [CrossRef]

21. Yu, W.; Xu, D.; Peng, T. Enhanced photocatalytic activity of g-C_3N_4 for selective CO_2 reduction to CH_3OH via facile coupling of ZnO: A direct Z-scheme mechanism. *J. Mater. Chem. A* **2015**, *3*, 19936–19947. [CrossRef]

22. Komatsu, T. The First Synthesis and Characterization of Cyameluric High Polymers. *Macromol. Chem. Phys.* **2001**, *202*, 19–25. [CrossRef]

23. Wu, P.; Wang, J.; Zhao, J.; Guo, L.; Osterloh, F.E. Structure defects in g-C_3N_4 limit visible light driven hydrogen evolution and photovoltage. *J. Mater. Chem. A* **2014**, *2*, 20338–20344. [CrossRef]

24. Papailias, I.; Giannakopoulou, T.; Todorova, N.; Demotikali, D.; Vaimakis, T.; Trapalis, C. Effect of processing temperature on structure and photocatalytic properties of g-C_3N_4. *Appl. Surf. Sci.* **2015**, *358*, 278–286. [CrossRef]

25. Horák, M.; Papoušek, D. *Infrared Spectra and Structure of Molecules*; Academia: Prague, Czech Republic, 1976.

26. Hariharan, C. Photocatalytic degradation of organic contaminants in water by ZnO nanoparticles: Revisited. *Appl. Catal. A* **2006**, *304*, 55–61. [CrossRef]

27. Zinin, P.V.; Ming, L.-C.; Sharma, S.K.; Khabashesku, V.N.; Liu, X.; Hong, S.; Endo, S.; Acosta, T. Ultraviolet and near-infrared Raman spectroscopy of graphitic C_3N_4 phase. *Chem. Phys. Lett.* **2009**, *472*, 69–73. [CrossRef]

28. Kuang, P.-Y.; Su, Y.-Z.; Chen, G.-F.; Luo, Z.; Xing, S.-Y.; Li, N.; Liu, Z.-Q. g-C_3N_4 decorated ZnO nanorod arrays for enhanced photoelectrocatalytic performance. *Appl. Surf. Sci.* **2015**, *358*, 296–303. [CrossRef]

29. Troppová, I.; Šihor, M.; Reli, M.; Ritz, M.; Praus, P.; Kočí, K. Unconventionally prepared TiO_2/g-C_3N_4 photocatalysts for photocatalytic decomposition of nitrous oxide. *Appl. Surf. Sci.* **2018**, *430*, 335–347. [CrossRef]

30. Li, J.; Zhang, M.; Li, Q.; Yang, J. Enhanced visible light activity on direct contact Z-scheme g-C_3N_4-TiO_2 photocatalyst. *Appl. Surf. Sci.* **2017**, *391*, 184–193. [CrossRef]

31. Liu, Y.; Wang, R.; Yang, Z.; Du, H.; Jiang, Y.; Shen, C.; Liang, K.; Xu, A. Enhanced visible-light photocatalytic activity of Z-scheme graphitic carbon nitride/oxygen vacancy-rich zinc oxide hybrid photocatalysts. *Chin. J. Catal.* **2015**, *36*, 2135–2144. [CrossRef]

32. Berks, B.C.; Ferguson, S.J.; Moir, J.W.; Richardson, D.J. Enzymes and associated electron transport systems that catalyse the respiratory reduction of nitrogen oxides and oxyanions. *Biochim. Biophys. Acta* **1995**, *1232*, 97–173. [CrossRef]

33. Troppová, I.; Matějová, L.; Sezimová, H.; Matěj, Z.; Peikertová, P.; Lang, J. Nanostructured TiO_2 and ZnO prepared by using pressurized hot water and their eco-toxicological evaluation. *J. Nanopart. Res.* **2017**, *19*, 198. [CrossRef]

34. Koci, K.; Reli, M.; Svoboda, L.; Praus, P. In Exfoliated nanosheets of graphitic carbon nitride: Study of optical and photoelectrochemical properties. In Proceedings of the 8th International Conference on Nanomaterials—Research & Application (NANOCON 2016), Brno, Czech Republic, 19–21 October 2016; Tanger Ltd.: Brno, Czech Republic, 2017; pp. 98–103.

35. Tasbihi, M.; Kočí, K.; Edelmannová, M.; Troppová, I.; Reli, M.; Schomäcker, R. Pt/TiO$_2$ photocatalysts deposited on commercial support for photocatalytic reduction of CO$_2$. *J. Photochem. Photobiol. A* **2018**, *366*, 72–80. [CrossRef]

36. Reli, M.; Troppová, I.; Šihor, M.; Pavlovský, J.; Praus, P.; Kočí, K. Photocatalytic decomposition of N$_2$O over g-C$_3$N$_4$/BiVO$_4$ composite. *Appl. Surf. Sci.* **2019**, *469*, 181–191. [CrossRef]